

Title	Loosely Coupled Simulation for Aortic Arch Model under Steady and Pulsatile Flow
Author(s)	GAO, Feng; GUO, Zhihong; WATANABE, Masahiro; MATSUZAWA, Teruo
Citation	Journal of Biomechanical Science and Engineering, 1(2): 327-341
Issue Date	2006
Type	Journal Article
Text version	publisher
URL	http://hdl.handle.net/10119/8502
Rights	Copyright (C) 2006 日本機械学会. Feng GAO, Zhihong GUO, Masahiro WATANABE, Teruo MATSUZAWA, Journal of Biomechanical Science and Engineering, 1(2), 2006, 327-341. http://dx.doi.org/10.1299/jbse.1.327
Description	

Loosely Coupled Simulation for Aortic Arch Model under Steady and Pulsatile Flow*

Feng GAO**, Zhihong GUO***, Masahiro WATANABE****, Teruo MATSUZAWA****

**Graduate School of Information Science, Japan Advanced Institute of Science and Technology
1-1 Asahidai, Nomi, Ishikawa, 923-1292, Japan

***Advanced Calculation Engineering Department, Surigiken Co. Ltd.
5-6-21 Kita-Shinagawa, Shinagawa-ku Tokyo 141-0001

****Center of Information Science, Japan Advanced Institute of Science and Technology
1-1 Asahidai, Nomi, Ishikawa, 923-1292, Japan

Abstract

Cardiovascular disease is the one of most important diseases for human in the developed countries and is responsible for millions of deaths and disabilities every year. In cardiovascular biomechanics, the fluid-structure interaction within large blood vessel is required to understand the aortic wall tear, aortic dissection and so on. Strongly-coupled methods yield the resolution of a nonlinear problem on the fluid-structure interface, which may be very time-consuming. A loosely coupled method was used to study the complex mechanical interaction under steady flow and pulsatile flow in a three-layered aortic arch model. The results showed the impact of steady flow and pulsatile flow, the variations of wall stress along arch portion, and wall stress distribution in three-layered wall.

Key words: Layered Wall, Loosely-Coupled Algorithms, Fluid-Structure Interaction, Cardiovascular, Aorta

1. Introduction

Cardiovascular disease is one of most important diseases for human in the developed countries and is responsible for millions of deaths and disabilities every year [1]. In cardiovascular biomechanics one of the major topics today is the simulation and analysis of the hemodynamics of the cardiovascular system using computational methods [2]. From the mechanical point of view, tear and dissection appear if the stresses acting on the wall rise above the ultimate value for the aorta wall tissue. Thubrikar et al. [3] proposed that longitudinal stress could be responsible for the tear in the aortic dissection. MacLean et al. [4] showed the role of radial tensile stress in aortic dissection. The simulation of the fluid-structure interaction (FSI) in large arterial vessel can provide the insight of a risk predictor for aortic wall tear, aortic dissection, and so on. The complexity of the geometry, motion, deformation and flows and their interactions make the simulation a major challenge.

There are many approaches attempting to solve the FSI problems. Generally the approaches for FSI can be differentiated into monolithic (strongly coupled) and staggered (loosely coupled) methods. For the first approach, it has been observed in many works [5, 6, 7] that strongly-coupled algorithms seem to be mandatory in blood flows. But strongly-coupled methods yield the resolution of a nonlinear problem on the fluid-structure interface [7], which may be very time-consuming. The staggered algorithms for fluid-structure problems are very efficient in aeroelasticity [8, 9]. The

loosely coupled methods have the advantages: they ensure that the fluid–structure solver will automatically inherit future improvements in fluid or structure algorithms [10]. Besides, the loosely coupled method can make utilization of high performance computing [11, 12], especially for some simulations that have intensive memory and CPU requirements.

In this paper, the complex mechanical interaction between blood flow and wall dynamics is simulated using the loosely-coupled algorithms. The computational fluid dynamics (CFD) and computational structure dynamics (CSD) equations are solved independently each other.

The human aorta has a characteristic configuration of the arch and the aorta wall is composed of three layers: the tunica intima (innermost), the tunica media (middle), and the tunica adventitia (outermost). So a three-layered aortic arch model is constructed to simulate the interaction between blood flow and wall dynamics. The stress distributions along the arch and in wall are analyzed.

2. Methods

A. Loosely Coupled Algorithm

In the fluid-structure interaction problem, fluid affects structure and also structure affects fluid. In this study, the procedure is based on loose coupling of three fields of problems: the flow, the elastic body, and the mesh movement – that is, the CFD (computation fluid dynamics), CSD (computational structural dynamics), and CMD (computational mesh dynamics) procedures.

The coupling strategy is first to solve the CFD and calculate the traction at the interface, second to apply fluid traction on the structure, solve the CSD, and obtain the displacement on interface, and then to impose the displacement of interface, solve the CMD, calculate the mesh velocity and impose the mesh velocity on CFD.

(i) Computational Fluid Dynamics (CFD)

The ALE (Arbitrary Lagrangian Eulerian) form of the Navier-Stokes equations is used to solve for fluid flow for FSI problems and calculate the traction at wetted surface that constitutes the boundary between the fluid and the structure. The equations governing the fluid (CFD) are:

$$\rho^F \frac{\partial u_i}{\partial t} + \rho^F u_{i,j} \cdot (u_j - \hat{u}_j) = \sigma_{ij,j}^F + \rho^F f_i^F \quad (1)$$

$$\frac{\partial \rho^F}{\partial t} + (\rho^F u_j)_{,j} = 0 \quad (2)$$

where u_i is the velocity, ρ^F is the fluid density, σ_{ij}^F is the fluid stress tensor, f_i^F is the body force at time t per unit mass, \hat{u} is the mesh velocity. For a nearly incompressible field the first term of the second equation is equal to zero. The boundary conditions can be expressed:

$$u_i = \bar{u}_i \quad \text{on } {}^U \Gamma(t) \quad (3)$$

where ${}^U \Gamma(t)$ is the velocity boundary condition and the tilde symbol ($\bar{\quad}$) denotes the prescribed values.

After spatial discretization by the finite element method, the Navier-Stokes equations are expressed in the ALE formulation:

$$\mathbf{M}\mathbf{a} + \mathbf{N}(\mathbf{v} - \hat{\mathbf{v}})\mathbf{v} + \mathbf{D}\mathbf{v} - \mathbf{C}\mathbf{p} = \mathbf{f} \quad (4)$$

$$\mathbf{C}^T \mathbf{v} = \mathbf{0} \quad (5)$$

where \mathbf{M} represents the fluid mass matrix; \mathbf{N} , \mathbf{D} , and \mathbf{C} are, respectively, the convective, diffusive, and divergence matrices; \mathbf{f} is an external body force; vectors \mathbf{a} , \mathbf{v} , and \mathbf{p} contain the unknown values of acceleration, velocity, and pressure, respectively.

Vectors \mathbf{a} , \mathbf{v} , and \mathbf{f} are expressed as

$$\mathbf{a}^T = \{^F \mathbf{a}^T, ^U \bar{\mathbf{a}}^T, ^I \mathbf{a}^T\}, \quad \mathbf{v}^T = \{^F \mathbf{v}^T, ^U \bar{\mathbf{v}}^T, ^I \mathbf{v}^T\}, \quad \mathbf{f}^T = \{^F \bar{\mathbf{f}}^T, ^U \mathbf{f}^T, ^I \mathbf{f}^T\} \quad (6)$$

where superscript (F) indicates values related to nodes placed in the fluid $^F \Omega(t)$, superscript (U) indicates values related to nodes on the boundary $^U \Gamma(t)$, superscript (I) indicates values related to the nodes on interface $^I \Gamma(t)$ between fluid and structure.

In the equation (6), the following compatibility conditions are already imposed on the interface:

$$\begin{aligned} ^F \mathbf{v} &= ^I \mathbf{v} \\ ^F \mathbf{a} &= ^I \mathbf{a} \end{aligned} \quad \text{on } ^I \Gamma(t) \quad (7)$$

Equation (4) can be partitioned as follows

$$\begin{aligned} & \begin{bmatrix} ^{FF} \mathbf{M} & ^{FU} \mathbf{M} & ^{FI} \mathbf{M} \\ ^{UF} \mathbf{M} & ^{UU} \mathbf{M} & ^{UI} \mathbf{M} \\ ^{IF} \mathbf{M} & ^{IU} \mathbf{M} & ^{II} \mathbf{M} \end{bmatrix} \begin{Bmatrix} ^F \mathbf{a} \\ ^U \bar{\mathbf{a}} \\ ^I \mathbf{a} \end{Bmatrix} + \begin{bmatrix} ^{FF} \mathbf{N} & ^{FU} \mathbf{N} & ^{FI} \mathbf{N} \\ ^{UF} \mathbf{N} & ^{UU} \mathbf{N} & ^{UI} \mathbf{N} \\ ^{IF} \mathbf{N} & ^{IU} \mathbf{N} & ^{II} \mathbf{N} \end{bmatrix} \begin{Bmatrix} ^F \mathbf{v} \\ ^U \bar{\mathbf{v}} \\ ^I \mathbf{v} \end{Bmatrix} \\ & + \begin{bmatrix} ^{FF} \mathbf{D} & ^{FU} \mathbf{D} & ^{FI} \mathbf{D} \\ ^{UF} \mathbf{D} & ^{UU} \mathbf{D} & ^{UI} \mathbf{D} \\ ^{IF} \mathbf{D} & ^{IU} \mathbf{D} & ^{II} \mathbf{D} \end{bmatrix} \begin{Bmatrix} ^F \mathbf{v} \\ ^U \bar{\mathbf{v}} \\ ^I \mathbf{v} \end{Bmatrix} - \begin{bmatrix} ^F \mathbf{C} \\ ^U \mathbf{C} \\ ^I \mathbf{C} \end{bmatrix} \mathbf{p} = \begin{Bmatrix} ^F \bar{\mathbf{f}} \\ ^U \mathbf{f} \\ ^I \mathbf{f} \end{Bmatrix} \quad (8) \end{aligned}$$

and the equation (5) can be expressed as

$$\begin{bmatrix} ^F \mathbf{C}^T & ^U \mathbf{C}^T & ^I \mathbf{C}^T \end{bmatrix} \begin{Bmatrix} ^F \mathbf{v} \\ ^U \bar{\mathbf{v}} \\ ^I \mathbf{v} \end{Bmatrix} = \mathbf{0} \quad (9)$$

In the loose coupling approach, the equations (8) (9) are rearranged so that they are explicit in the fluid unknowns. Thus:

$$\begin{aligned} & ^{FF} \mathbf{M} ^F \mathbf{a} + ^{FF} \mathbf{N} ^F \mathbf{v} + ^{FF} \mathbf{D} ^F \mathbf{v} - ^F \mathbf{C} \mathbf{p} = ^F \bar{\mathbf{f}} - \begin{bmatrix} ^{FU} \mathbf{M} & ^{FI} \mathbf{M} \\ ^{UF} \mathbf{M} & ^{UI} \mathbf{M} \end{bmatrix} \begin{Bmatrix} ^U \bar{\mathbf{a}} \\ ^I \mathbf{a} \end{Bmatrix} \\ & + \begin{bmatrix} ^{FU} \mathbf{N} & ^{FI} \mathbf{N} \\ ^{UF} \mathbf{N} & ^{UI} \mathbf{N} \end{bmatrix} \begin{Bmatrix} ^U \bar{\mathbf{v}} \\ ^I \mathbf{v} \end{Bmatrix} - \begin{bmatrix} ^{FU} \mathbf{D} & ^{FI} \mathbf{D} \\ ^{UF} \mathbf{D} & ^{UI} \mathbf{D} \end{bmatrix} \begin{Bmatrix} ^U \bar{\mathbf{v}} \\ ^I \mathbf{v} \end{Bmatrix} \quad (10) \end{aligned}$$

$$^F \mathbf{C}^T ^F \mathbf{v} = -^U \mathbf{C}^T ^U \bar{\mathbf{v}} - ^I \mathbf{C}^T ^I \mathbf{v} \quad (11)$$

The load applied by the fluid on the elastic body along the interface is obtained:

$$\begin{aligned}
 {}^I \mathbf{f} = & \left[{}^{IF} \mathbf{M} \quad {}^{IU} \mathbf{M} \quad {}^{IF} \mathbf{M} \right] \begin{Bmatrix} {}^F \mathbf{a} \\ {}^U \mathbf{a} \\ {}^I \mathbf{a} \end{Bmatrix} + \left[{}^{IF} \mathbf{N} \quad {}^{IU} \mathbf{N} \quad {}^{IF} \mathbf{N} \right] \begin{Bmatrix} {}^F \mathbf{v} \\ {}^U \mathbf{v} \\ {}^I \mathbf{v} \end{Bmatrix} \\
 & + \left[{}^{IF} \mathbf{D} \quad {}^{IU} \mathbf{D} \quad {}^{IF} \mathbf{D} \right] \begin{Bmatrix} {}^F \mathbf{v} \\ {}^U \mathbf{v} \\ {}^I \mathbf{v} \end{Bmatrix} - {}^I \mathbf{Cp} = -{}^I \mathbf{t} \quad (12)
 \end{aligned}$$

where ${}^I \mathbf{t}$ is the traction applied by the fluid on the elastic body along the interface between fluid and structure. Equation (12) is an expression of Newton's third law.

(ii) Computational Structural Dynamics (CSD)

The overall structural behavior is described by the momentum equation (13), the equilibrium equation (14) and the constitutive equations (15) (16):

$$\rho^S \ddot{d}_i = \sigma_{ij,j}^S + \rho^S \bar{f}_i^S \quad \text{in } {}^S \Omega(t) \quad (13)$$

$$\sigma_{ij}^S n_j^S = {}^I \bar{t}_i \quad \text{on } {}^I \Gamma(t) \quad (14)$$

$$\sigma_{ij}^S = D_{ijkl} \varepsilon_{kl} \quad \text{in } {}^S \Omega(t) \quad (15)$$

$$\varepsilon_{kl} = \frac{1}{2} (d_{k,l} + d_{l,k}) \quad \text{in } {}^S \Omega(t) \quad (16)$$

where ${}^I \bar{t}_i$ is the surface traction vector calculated in CFD, ρ^S is the density of the structural material, \ddot{d}_i is the acceleration of a material point (where displacement is defined as $d_i = x_i - x_{i0}$, and x_{i0} is the stress-free position), σ_{ij}^S is the stress tensor in the structural domain, \bar{f}_i^S is the externally applied body force vector, ${}^S \Omega(t)$ is the structural domain, n_j^S is the outward pointing normal on ${}^S \Gamma(t)$, D_{ijkl} is the material (lagrangian) elasticity tensor, and ε_{kl} is the infinitesimal strain tensor. The wall deformation is thus governed by the principle of virtual displacements

$$\int_{{}^S \Omega(t)} \rho^S \ddot{d}_i \delta d_i d\Omega + \int_{{}^S \Omega(t)} d_{,j} \delta d_{i,j} d\Omega = \int_{{}^S \Omega(t)} \rho^S \bar{f}_i \delta d_i d\Omega + \int_{{}^I \Gamma(t)} {}^I \bar{t}_i \delta d_i d\Gamma \quad (17)$$

where δd_i is the virtual displacement vector.

Boundary conditions for structural domain take the following form:

$$d_i = \bar{d}_i \quad \text{on } {}^d \Gamma \quad (18)$$

$$f_i = \bar{f}_i \quad \text{on } {}^\sigma \Gamma \quad (19)$$

where ${}^d \Gamma$ is the displacement condition, ${}^\sigma \Gamma$ is the stress boundary condition.

Initial conditions for structural domain take the following form:

$$\left. \begin{aligned} d_i &= \bar{d}_i^0 \\ \dot{d}_i &= \bar{\dot{d}}_i^0 \end{aligned} \right\} \quad \text{in } {}^F\Omega(0) \quad (20)$$

The corresponding matrix equation for structure can be written as

$${}^S\mathbf{M} {}^S\mathbf{a} + {}^S\mathbf{K} {}^S\mathbf{d} = {}^S\bar{\mathbf{f}} + {}^I\bar{\mathbf{t}} - {}^\sigma\mathbf{f} \quad (21)$$

where ${}^S\mathbf{M}$, ${}^S\mathbf{K}$ are, respectively, the structural mass, nonlinear stiffness matrices; ${}^S\bar{\mathbf{f}}$ is the external body force vector, ${}^I\bar{\mathbf{t}}$ is the traction applied by the fluid on the interface, ${}^\sigma\mathbf{f}$ is the force due to the internal stresses at the most recently calculated configuration, ${}^\sigma\mathbf{f}$ is zero for steady problem but not zero for unsteady problem; ${}^S\mathbf{d}$ is the vector of increments in the nodal point displacement; and ${}^S\mathbf{a}$ is the vector of nodal point acceleration. The equation of motion can be integrated and the displacement, velocity, and acceleration vectors can be calculated:

$${}^S\mathbf{d}_{n+1} = {}^S\mathbf{d}_{n+1} + \Delta t {}^S\mathbf{v}_n + \frac{1}{2}(\Delta t)^2 {}^S\mathbf{a}_n + \beta(\Delta t)^2 ({}^S\mathbf{a}_{n+1} - {}^S\mathbf{a}_n) \quad (22)$$

$${}^S\mathbf{v}_{n+1} = {}^S\mathbf{v}_n + \Delta t [(1 - \gamma) {}^S\mathbf{a}_n + \gamma {}^S\mathbf{a}_{n+1}] \quad (23)$$

$${}^S\mathbf{M} {}^S\mathbf{a}_{n+1} + {}^S\mathbf{K} {}^S\mathbf{d}_{n+1} = ({}^S\bar{\mathbf{f}} + {}^I\bar{\mathbf{t}} - {}^\sigma\mathbf{f})_{n+1} \quad (24)$$

In these equations, β and γ are integration parameters that can be adjusted to achieve numerical accuracy and stability. The displacement at interface between fluid and structure is:

$${}^I\mathbf{d} = {}^S\mathbf{d} \quad \text{on } {}^I\Gamma(t) \quad (25)$$

The displacement at interface is input to CMD to determine the fluid mesh displacement.

(iii) Computational Mesh Dynamics (CMD)

The remeshing algorithm employs a scalar distortion parameter, $\tilde{\Phi}_{el}^i$, as an element quality indicator. The normalized distortion parameter is defined as

$$\tilde{\Phi}_{el}^i = \Phi_{el}^i / \Phi_{el}^0 \quad (26)$$

where el denotes element number, i is the iteration count, and 0 represents the initial mesh. The Young's modulus of each element in the mesh is calculated as

$$\hat{E}_{el} = \hat{E}^0 (\tilde{\Phi}_{el}^i)^n \quad (27)$$

where \hat{E}^0 is an elasticity modulus input by the user, n is a parameter to determine the stiffness of the element. The value of n can range between 0 and 10. Zero represents no stiffening and 10 represents maximum stiffness. The value of 2 was used due to the typical value for power coefficient for hexahedral element in the present study.

The elasticity-based model is used to determine the mesh displacement and update the mesh geometry. The mesh is treated as an elastostatic structure upon which stresses are imposed by virtue of the movement of the structure. The displacements are obtained

from

$$\hat{\mathbf{K}}\hat{\mathbf{d}} = \mathbf{0} \quad (28)$$

where $\hat{\mathbf{K}}$ is the stiffness matrix, and $\hat{\mathbf{d}}$ is the mesh displacement vector defined by

$$\hat{\mathbf{d}} = \hat{\mathbf{R}}(t) - \hat{\mathbf{R}}(\hat{t}_{ref}) \quad (29)$$

where $\hat{\mathbf{R}}$ is the mesh position vector, and \hat{t}_{ref} is the reference time.

The equation (28) can be rewritten in a partitioned form as

$$\begin{bmatrix} {}^{FF}\hat{\mathbf{K}} & {}^{FI}\hat{\mathbf{K}} \\ {}^{IF}\hat{\mathbf{K}} & {}^{II}\hat{\mathbf{K}} \end{bmatrix} \begin{Bmatrix} {}^F\hat{\mathbf{d}} \\ {}^I\hat{\mathbf{d}} \end{Bmatrix} = \begin{Bmatrix} \mathbf{0} \\ \mathbf{0} \end{Bmatrix} \quad (30)$$

On the interface between fluid and structure, the mesh displacement is imposed according to the boundary conditions:

$$\hat{\mathbf{d}} = {}^I\hat{\mathbf{d}} \quad (31)$$

So we obtain

$${}^{FF}\hat{\mathbf{K}}^F\hat{\mathbf{d}} = -{}^{FI}\hat{\mathbf{K}}^I\hat{\mathbf{d}} \quad (32)$$

which shows that the fluid mesh motion is driver by the elastic body motion. This equation, together with the other boundary condition, is solved for the fluid mesh displacement. After it is remeshed, it starts the new loop from CFD.

B. Geometry of Aortic Arch

The aorta is the largest artery in the human body. It consists of the ascending aorta, the aortic arch, and the descending aorta. A radius of the arch was set to be 0.03m and the diameter of vessel was assumed to be uniform (0.024m). The average diameter of aorta is 0.02-0.025m [13]. All the major branches of the arch were neglected as a first order approximation. The thickness of whole wall was chosen to be 0.002m. The thickness of the aortic wall was 0.002m on postmortem computed tomography in Shiotani's [14] paper. Fig. 1 shows the geometry of analysis model including finite element mesh described.

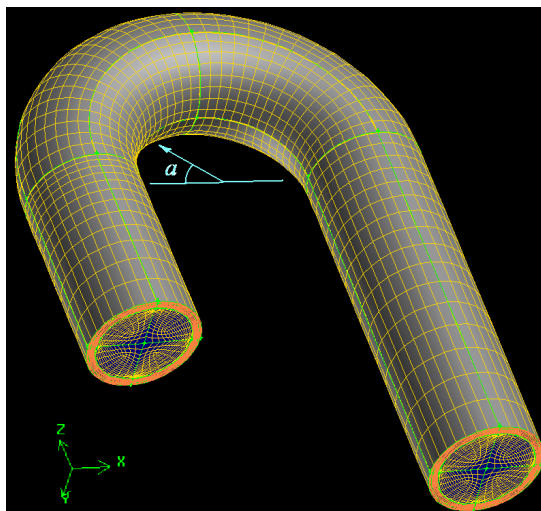


Fig. 1 Geometry of analysis model including finite element mesh described. The angle α represents the wall position in the median longitudinal cross-section.

C. Properties of Wall Layers

The three-layered wall model as well as intact wall model was conducted in this study.

(i) One-layered wall model

The thickness of intact wall was set to $t=0.002\text{m}$. The elastic properties of aorta wall were determined by Young's modulus. In this study, the aortic arch is a self-supporting structure. The $E=6.5\text{MPa}$ [15] was chosen for the Young's modulus of aorta wall. Poisson's ratio is set 0.45 as nearly incompressible material.

(ii) Three-layered wall model

In this three-layered wall model, the thickness ratio of intima/media/adventitia was set to 1/6/3 based on [16]. In this present study, the Young's modulus of media layer is assumed three times larger than that of adventitia layer and that of intima layer base on the literature [17, 18, 19, 20]. Since the mean Young's modulus of vessel wall is same, we assume that the Young's modulus of layer is in inverse proportion to the area of layer, thus:

$$E \cdot A = E_i \cdot A_i + E_m \cdot A_m + E_a \cdot A_a \quad (33)$$

where A_i, A_m, A_a and A are the area of intima layer, media layer, adventitia layer and whole wall, respectively. We assume the vessel is straight, so using the volume equation, the equation (33) becomes:

$$\begin{aligned} & E \cdot [2rt + t^2] \\ &= E_i \cdot [2rt_i + t_i^2] + E_m \cdot [2(r + t_i)t_m + t_m^2] \\ & \quad + E_a \cdot [2(r + t_i + t_m)t_a + t_a^2] \end{aligned} \quad (35)$$

where r is the radius of the lumen. We can obtain the Young's modulus of intima layer, media layer, and adventitia layer: $E_i=2.984140\text{MPa}$, $E_m=8.952421\text{MPa}$, $E_a=2.984140\text{MPa}$. Wall's Poisson coefficient is set 0.45 in both models.

D. Properties of Fluid and Boundary Condition

The surface of the inlet channel was fixed. The outer edge of outlet was constrained in the axial direction and permitted to move in the other directions.

The fluid is Newtonian with a density of 1050 kg/m^3 and a viscosity of $0.0035\text{ Pa}\cdot\text{s}$. The Newtonian assumption has been considered acceptable since minor differences in the basic flow characteristics are introduced through the non-Newtonian hypothesis [21].

(i) Steady inflow condition

The Reynolds number of inlet flow was fixed at $Re=1350$ and $Re=4000$. The time average Reynolds numbers over a whole cycle is $Re=1350$ in the ascending aorta taken from Liepsch's [22] measurements of the flow in a human aortic arch. The typical Reynolds number for blood flow is approximately $Re=4000$ in the aorta [23].

(ii) Usteady inflow condition

At the aortic inlet, a flat flow velocity profile was used together with pulsatile waveform based on reported experimental data by [24, 25]. In our calculations, the Reynolds number is fixed at $Re=4000$ based on the inlet velocity at peak systole of the cardiac cycle. At the beginning of the simulation, the iteration has large errors and three cardiac cycles have been simulated in order to achieve a periodically convergent

solution independent from the initial conditions.

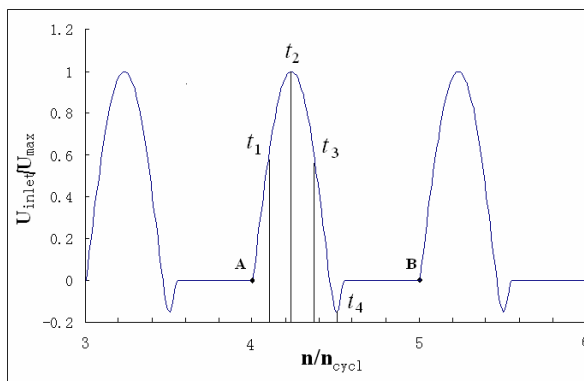


Fig. 2 Inlet velocity profile. n is the time step, n_{cycl} is the total time steps in one cycle. For the final run, the cardiac cycle is started at A and ends at B.

3. Results

A. Steady Inflow Condition

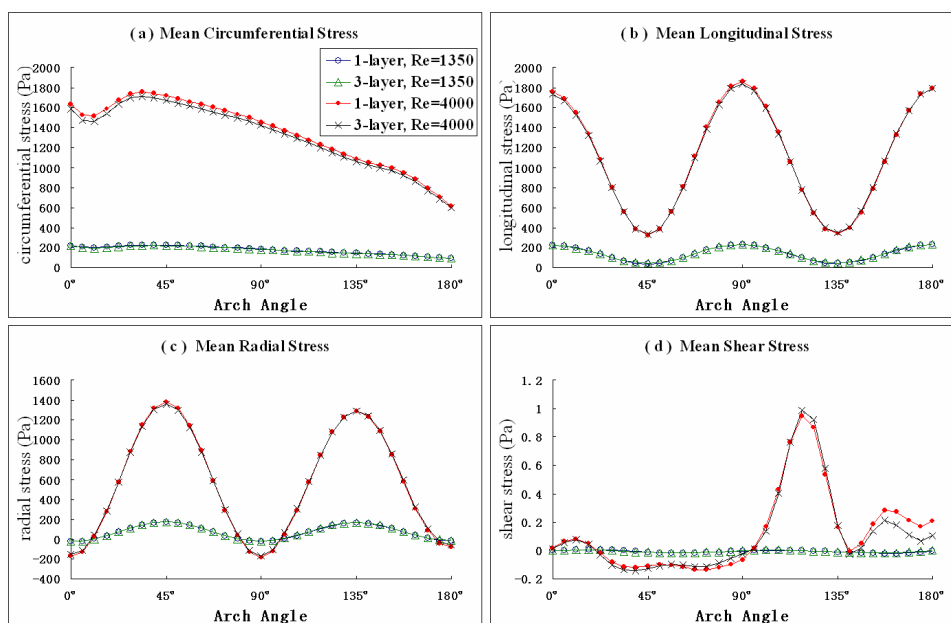


Fig. 3. The mean stresses distribution in outer wall in the one-layered and three-layered model along the arch portion at $Re=1350$ and $Re=4000$. The mean circumferential stress distribution (a). The mean longitudinal stress distribution (b). The mean radial stress distribution (c). The mean shear stress distribution (d).

The variations of mean stresses on outer wall along the arch at the inlet flow Reynolds number of $Re=1350$ and $Re=4000$ for the one-layered model and the three-layered model are shown in Fig. 3. The mean stress is average stress of transverse cross wall.

The stress at $Re=4000$ is higher than that at $Re=1350$. The variations of circumferential, longitudinal, and radial stress at $Re=1350$ and $Re=4000$ have a similar pattern. The circumferential stress gets a minor peak at the mid ascending portion and then decreases along the arch. For longitudinal stress, the peak values are at the entrance ascending portion, the top of the arch and the distal end of arch. The radial

stress gets a peak value at the mid ascending portion and the mid descending portion.

The shear stress at $Re=4000$ is much higher than that at $Re=1350$. At $Re=4000$ the variation of shear stress is not regular and the shear stress is higher at the descending portion than at the ascending portion.

B. Pulsatile Inflow Condition

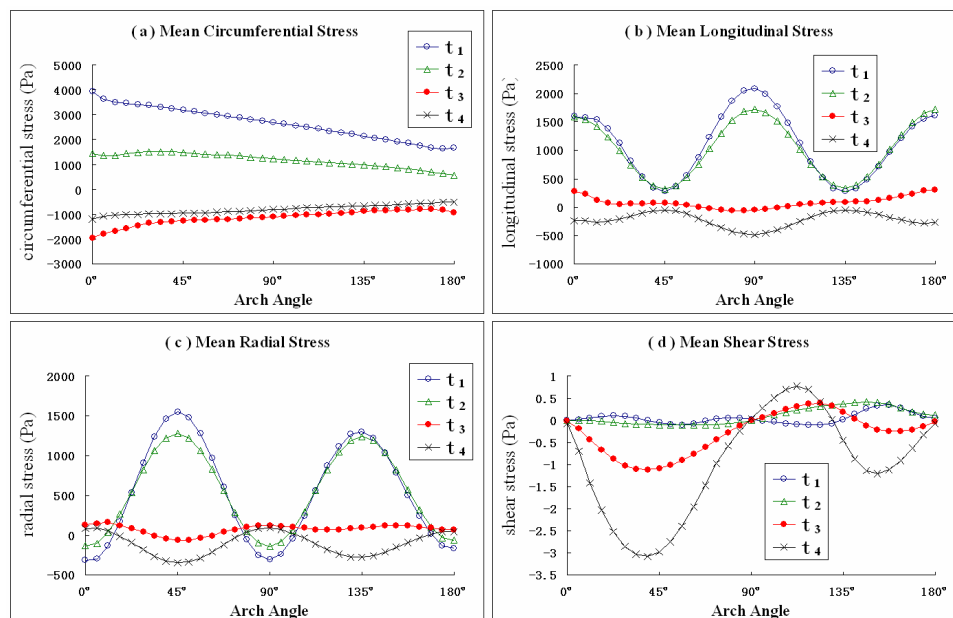


Fig. 4. The mean stress distribution in outer wall in the three-layered model along the arch portion. The circumferential stress distribution (a). The longitudinal stress distribution (b). The radial stress distribution (c). The shear stress distribution (d). t_1 : systolic acceleration, t_2 : peak entrance flow, t_3 : systolic deceleration, and t_4 : foot entrance flow.

1. Variations of stresses along arch

Fig. 4 presents the variations of the mean circumferential stress, the mean longitudinal stress, the mean radial stress and the mean shear stress in outer wall along arch at systolic acceleration (t_1), peak entrance flow (t_2), systolic deceleration (t_3), and foot entrance flow (t_4) in the three-layered model. The circumferential, longitudinal, and radial stress at systolic acceleration (t_1) are highest among those at four different times. The shear stress at foot entrance flow (t_4) is highest among those at four different times.

The value of the circumferential stress decreases along the arch. At peak entrance flow (t_2), the circumferential stress gets a minor peak at the mid ascending portion and then decreases along the arch.

The longitudinal stress at systolic acceleration (t_1) and peak entrance flow (t_2) is much higher than that at systolic deceleration (t_3) and foot entrance flow (t_4). At systolic acceleration (t_1) and peak entrance flow (t_2), the peak values are at the entrance ascending portion, the top of the arch and the distal end of arch.

The radial stress at systolic acceleration (t_1) and peak entrance flow (t_2) is much higher than that at systolic deceleration (t_3) and foot entrance flow (t_4). At systolic acceleration (t_1) and peak entrance flow (t_2), the radial stress is a positive value in both the ascending and descending portions and the radial stress gets a peak value at the mid ascending portion and the mid descending portion.

For shear stress, the negative sign means the direction of stress. The shear stress at systolic deceleration (t_3) and foot entrance flow (t_4) is much higher than that at systolic acceleration (t_1) and peak entrance flow (t_2). At foot entrance flow (t_4), the shear stress gets a first peak value at the mid ascending portion and a second peak value at the back descending portion.

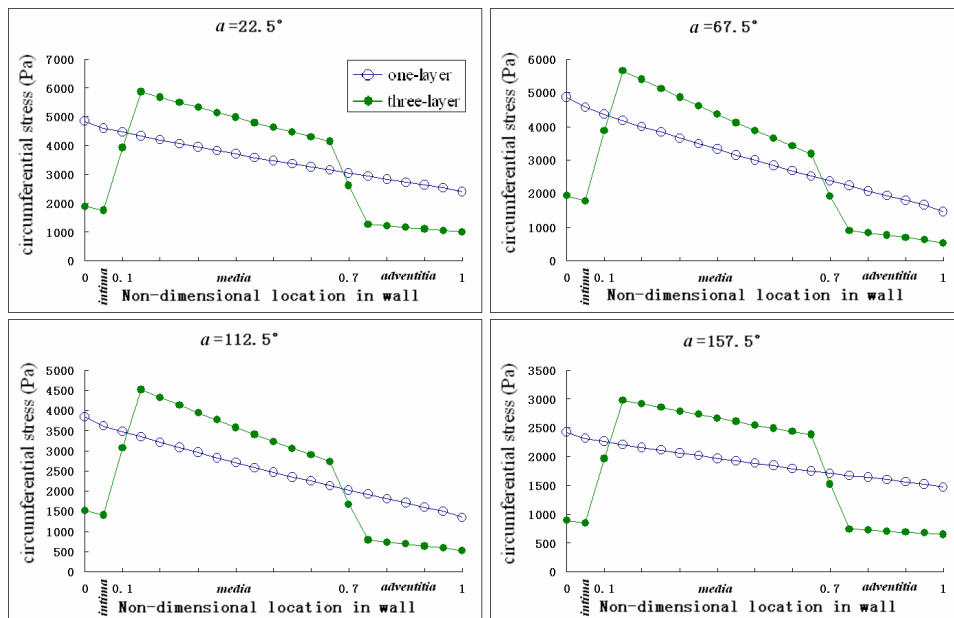


Fig. 5. Variation of the circumferential stress across the wall at systolic acceleration (t_1)

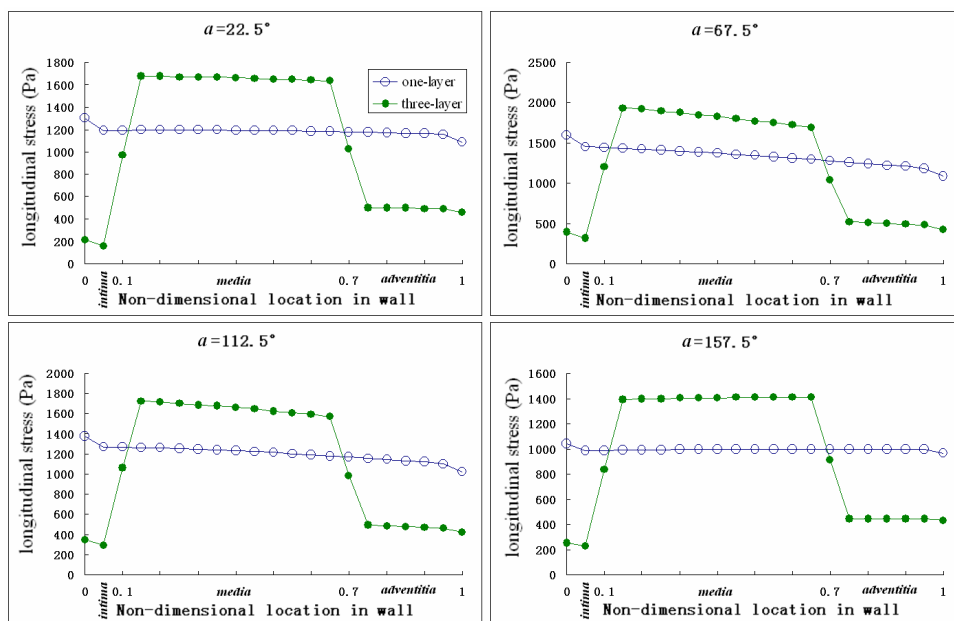


Fig. 6. Variation of the longitudinal stress across the wall at systolic acceleration (t_1)

2 Variations of stresses across the wall

Four positions $a=22.5^\circ$, $a=67.5^\circ$, $a=112.5^\circ$, and $a=157.5^\circ$ were selected in the arch portion to illustrate the variation of stresses across the wall.

For circumferential stress, longitudinal stress, and radial stress, t_1 (systolic acceleration) was selected since the value of stresses is highest at systolic acceleration (t_1) among the four times. For shear stress, t_4 (foot entrance flow) was selected since the value of stresses is highest at foot entrance flow (t_4) among the four times.

The variations of the circumferential stress across the one-layer model wall and the three-layer model wall at four positions at systolic acceleration (t_1) are shown in Fig. 5. Fig. 5 indicates a decreasing trend for circumferential stress with increasing radius in the 1-layer model. For the 3-layer model, the circumferential stress is much higher in the media layer than in the intima and adventitia layers. The variations of longitudinal and radial stress across the walls of the three models at four positions at systolic acceleration (t_1) are shown in Fig. 6 and Fig. 7. For the 3-layer model, longitudinal and radial stress are much higher in the media layer than in the intima and adventitia layers.

Variations of shear stress across the walls of the three models at four positions at foot entrance flow (t_4) are shown in Fig. 8. The shear stress is nonlinear distributed across wall thickness and higher in media.

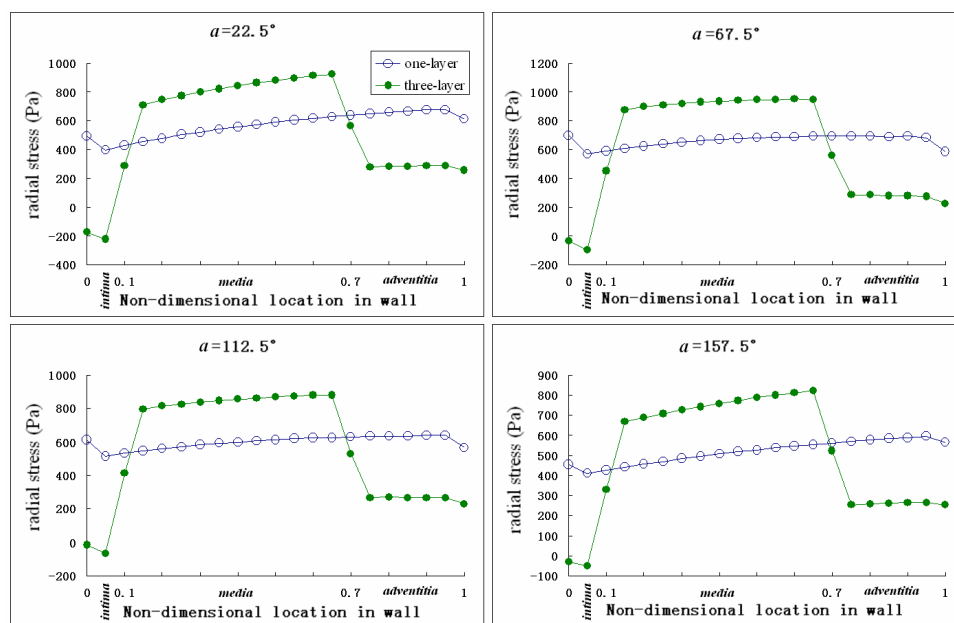


Fig. 7. Variation of the radial stress across the wall at systolic acceleration (t_1)

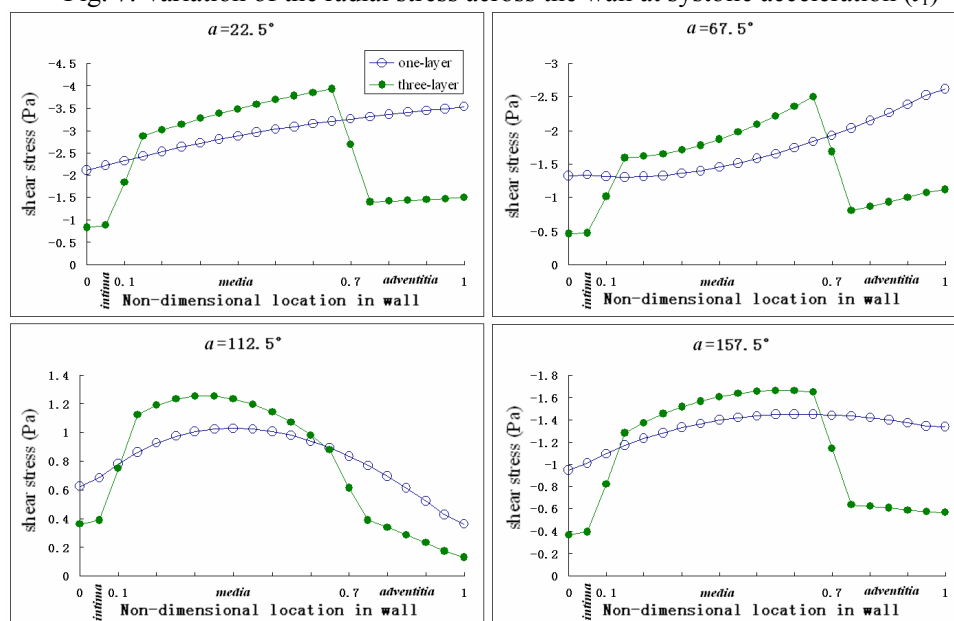


Fig. 8. Variation of the shear stress across the wall at foot entrance flow (t_4)

4. Discussion and Conclusion

The present study provides the simulation of FSI within layered aortic arch model under steady flow and pulsatile flow using a loosely coupled method. The stress distributions along the arch and in wall under steady flow and pulsatile flow are provided. At steady inflow condition, the higher is the flow rate the higher is the stress. Under pulsatile flow, the highest normal stress appears at systolic acceleration phase and the highest shear stress appears at foot entrance flow.

Wall stress is an important factor in aortic dissection, which has been recently addressed by several authors [3, 4, 26, 27, 28]. The variations of circumferential, longitudinal, and radial stress along arch at steady flow condition and at systolic acceleration (t_1), peak entrance flow (t_2) of pulsatile flow have a similar pattern.

Circumferential stress was considered an important parameter for the mechanosensitive receptors. In general, the higher is the fluid flow the higher is the wall stress. In the present study, the circumferential stress depicted in Fig. 4 (a) is higher at systolic acceleration phase (t_1) than that at peak entrance flow (t_2). So the systolic acceleration phase is more critical than the peak flow for risk of wall tear or dissection. Hence during the cardiac cycle, at systolic acceleration phase the circumferential stress may contribute to the tear on aortic wall.

In aortic dissection, the intimal tear is five times more likely to be transverse than longitudinal [29] and in some series it is reported to be transverse 95% of the time [30]. Thubrikar et al. [3] have proposed that longitudinal stress could be responsible for transverse tears in the aortic dissection. Roberts [31] reported that the tear is located in the ascending aorta, usually about 2 cm cephalad to the sinotubular junction, in 62% of the patients. This means the location is about at the entrance to the ascending portion of the arch. After the ascending aorta, about 16% of tears are at the aortic isthmus portion [31], which is near the top of the arch.

Under steady flow and at systolic acceleration phase (t_1) and peak entrance flow (t_2) of pulsatile flow, the longitudinal stress gets its peak values at the entrance to the ascending portion and the top of the arch. Yet, the longitudinal stress also peaks in the distal end of the arch, and tears do not often occur at this location. From Fig. 3 (a)(b) and Fig. 4 (a) (b) we can see that both circumferential stress decreases along the arch. Carsten [28] has mentioned that both circumferential stress and longitudinal stress create the risk of aortic dissection. Circumferential stress and longitudinal stress should be considered together for understanding of the intimal tear.

Under steady flow and at systolic acceleration phase (t_1) and peak entrance flow (t_2) of pulsatile flow the radial stress is a positive value in the ascending and descending portions, and thus, by definition, is tensile stress. Under normal conditions, radial stresses are compressive. MacLean et al. [4] showed that the aorta tore radially at a much lower value of radial tensile stress and mentioned that once a false lumen is formed by a dissection, radial tensile forces must exist in the aortic wall. In the present study, radial tensile stress exists due to the structure of arch and deformations of the wall. With dissections beginning in the ascending portion, the tear usually involves the right lateral aortic wall (outer wall) and thereafter courses downstream along the greater curvature of the ascending, transverse, and the descending thoracic portions of aorta [31]. Fig. 3 and Fig. 4 show the radial stress is high both in the ascending and descending portions at systolic acceleration phase (t_1) and peak entrance flow (t_2), and this can explain why most ascending aortic dissections extend to involve the descending aorta.

Many researchers have proposed that wall stress causes the tears and dissection in aortic dissection. For the 3-layer model of the aorta, all the stresses are highest in the media layer are highest in our numerical experiment. The results of Maltzahn et al. [18] also indicated the media was subject to much higher stresses. The stress in the intima layer is low, intima layer acting as a cushion in the aorta mechanics. Macleod and Soames [32] have shown that the distribution of these intimal cushions may be related to haemodynamic stress. The intima layer plays a protective role with respect to the aorta wall. Once an intimal tear occurs, it readily extends into the media layer since the stresses in the media layer are highest. The phenomenon in aortic dissection is that about 65 to 87% of aortic dissections occur in the ascending aorta [29,31,33] and the dissection spreads in the media.

The wall stresses and the breaking strength of the tissue must be considered together for understanding the aortic dissection. Despite the more accurate predictions of biomechanics utilizing an FSI technology, there are additional limitations. The external forces induced by surrounding tissue and organs, the variable thickness, the branches of aorta are related to the quantitative analysis. Due to the limitation of this technology we could not give quantities of strength of vessel wall. In the future work, we will include the additional factor to give a quantitative analysis. The material property of vessel wall is anisotropy and Wolinsky et al. [34] originated the phrase "Medial Lamellar Unit" (MLU) for a basic repetitive structural unit within the tunica media. Although the strength of the laminated arrangement makes the aorta durable enough to last for many years in a physiological environment, laminated structures are prone to split, creating a cleavage plane between lamellae. Van Baardwijk and Roach [35] suggested that the materials holding adjacent lamellae together are weaker than the elastin layers themselves.

Under steady flow, the higher is inflow velocity the higher shear stress. However, under pulsatile flow, the shear stress is highest at foot entrance flow or diastolic phase among those at four different times. So at foot entrance flow or diastolic phase, the shear stress may contribute to the aortic dissection.

In summary, the fluid-structure interaction within a 3-layered aortic arch model was simulated using a loosely coupled method to evaluate the impact of steady flow and pulsatile flow, calculate variations of wall stress along arch portion, determine wall stress distribution in three-layered wall, and provide insight into the biomechanics of aortic dissection. To the authors' knowledge, this is the first computation FSI study of 3-layered aortic arch model. As a future research, FSI simulation for the more complex aortic arch model and the more complex simulation condition on high performance computer is considered.

Acknowledgment

This research is conducted as a program for the "Fostering Talent in Emergent Research Fields" in Special Coordination Funds for Promoting Science and Technology by Ministry of Education, Culture, Sports, Science and Technology.

References

- [1] Tang, D. et al., "3D Computational Mechanical Analysis for Human Atherosclerotic Plaques Using MRI-Based Models with Fluid-Structure Interactions", *Lecture Notes in Computer Science*, Vol. 3217, (2004), pp. 328 –

- 336.
- [2] Taylor, C.A., “Predictive Medicine: Computational Techniques in Therapeutic decision-making”, *Computer Aided Surgery*, Vol.4, (1999), pp.231-247.
 - [3] Thubrikar, M.J. et al., “Wall Stress as A Possible Mechanism for the Development of Transverse Intimal Tears in Aortic Dissections”, *J. Med. Eng. Tech.*, Vol. 23, (1999), pp. 127-134.
 - [4] MacLean, N.F. et al., “The Role of Radial Elastic Properties in the Development of Aortic Dissections”, *J. Vasc. Surg.*, Vol. 29, (1999), pp. 703-710.
 - [5] Deparis, S. et al., “Acceleration of A Fixed Point Algorithm for A Fluid–structure Interaction Using Transpiration Conditions”, *Math. Model. Numer. Anal.*, Vol. 37, (2003), pp. 601–616.
 - [6] Gerbeau, J.F. and Vidrascu, M., “A Quasi-Newton Algorithm Based on A Reduced Model for Fluid–structure Interactions Problems in Blood Flows”, *Math. Model. Numer. Anal.*, Vol. 37, (2003), pp. 631–648.
 - [7] Tallec, P. L. and Mouro, J., “Fluid Structure Interaction with Large Structural Displacements”, *Comput. Meth. Appl. Mech. Engng.*, Vol. 190, (2001), pp. 3039–3067.
 - [8] Lesoinne, M. and Farhat, C., “Higher-order Subiteration-free Staggered Algorithm for Nonlinear Transient Aeroelastic Problems”, *AIAA J.*, Vol. 36, (1998), pp. 1754–1757.
 - [9] Piperno, S. et al., “Partitioned Procedures for the Transient Solution of Coupled Aeroelastic problems. Part I: Model problem, theory and two-dimensional application”, *Comp. Meth. Appl. Mech. Engng.*, 124, (1995), pp. 79–112.
 - [10] Gerbeau, J.F. et al., “Fluid–structure Interaction in Blood Flows on Geometries Based on Medical Imaging”, *Computers & Structures*, Vol. 83, No. (2-3), (2005), pp. 155-165.
 - [11] Halfmann, A. et al., “A Geometric Model for Fluid-structure Interaction of Wind-exposed Structure”, The Ninth International Conference on Computing in Civil and Building Engineering, 2002-4.
 - [12] Lee, S.H., Youn, S.K., Yeon, J.H., Jiang B.N., “A Study on Fluid-Structure Interaction using LSFEM”, *MSN2000*, pp. 548-552
 - [13] Engel, N., “Abdominal Aortic Aneurysm and Low Back Pain”, *Dynamic Chiropractic*, Vol. 14, No.16, 1996.
 - [14] Shiotani, S. et al., “Hyperattenuating Aortic Wall on Postmortem Computed Tomography”, *Radiation Medicine*, Vol. 20 No.4, (2002), pp. 201-206.
 - [15] Mosora, F., et al., “Modelling the Arterial Wall by Finite Elements”, *Arch. Int. Physiol. Biochim. Biophys.*, Vol. 101, No.3, 1993, pp. 185-191
 - [16] Schulze-Bauer, C.A. et al., “Passive Biaxial Mechanical Response of Aged Human Iliac Arteries”, *J. Biomech. Eng.*, Vol. 125, No.3, (2003), 395-406
 - [17] Maltzahn, W.W.V. et al., “Elastic Properties of Arteries: A Nonlinear Two-layer Cylindrical Model”, *J. Biomech.*, Vol. 14, (1981), pp.389-397.
 - [18] Maltzahn, W.W.V. et al., “Experimental Measurements of Elastic Properties of Media and Adventitia of Bovine Carotid Arteries”, *J. Biomech.*, Vol.17, (1984), pp.839-848.
 - [19] Xie, J. et al., “Bending of Blood Vessel Wall: Stress-strain Laws of the Intima-media and Adventitial Layers”, *J. Biomech. Eng.*, Vol.117, (1995), pp.136-145.
 - [20] Fischer, E.I. et al., “Endothelium-dependent Arterial Wall Tone Elasticity Modulated by Blood Viscosity”, *Am. J. Physiol. Heart Circ. Physiol.*, Vol.282, (2002), pp.389-394.
 - [21] Liepsch, D. et al., “Some Flow Visualization and Laser-Doppler Velocity

- Measurements in A True-to-scale Elastic Model of a Human Aortic Arch—A New Model Technique”, *Biorheology*, Vol.29, (1992), pp.563-580.
- [22]Liepsch, D. et al., “Some Flow Visualization and Laser-Doppler Velocity Measurements in A True-to-scale Elastic Model of A Human Aortic Arch—A New Model Technique”, *Biorheology*, Vol.29, (1992), pp.563-580.
- [23]Ku, D.N., “Blood Flow in Arteries”, *Annu. Rev. Fluid Mech.*, Vol.29, (1997), pp.399-434.
- [24]Pedley, T.J., *The Fluid Mechanics of Large Blood Vessels*, (1980), Cambridge University Press.
- [25]Nerem, R.M., “Vascular Fluid Mechanics, the Arterial Wall, and Atherosclerosis”, *J. Biomech. Eng.*, Vol.114, (1992), pp. 274–282.
- [26]Angouras, D. et al., “Effect of Impaired Vasa Vasorum Flow on the Structure and Mechanics of the Thoracic Aorta: Implications for the Pathogenesis of Aortic Dissection”, *Eur. J. Cardio- Thorac. Surg.*, Vol.17, (2000), pp.468–473.
- [27]Okamoto, R.J. et al., “The Influence of Mechanical Properties on Wall Stress and Distensibility of the Dilated Ascending Aorta”, *J. Thorac. Cardiovasc. Surg.*, Vol.126, (2003), pp.842-850.
- [28]Carsten, J.B. et al., Francis and H. Siegfried, “Increased Aortic Wall Stress in Aortic Insufficiency: Clinical Data and Computer Model”, *Eur. J. Cardio-Thorac. Surg.*, Vol.27, (2005), pp.270-275.
- [29]Doroghazi, R.M. et al., *Aortic Dissection*, (1983), pp.38, New York: McGraw-Hill Book Company.
- [30]Hirst, A. et al., “Dissecting Aneurysms of the Aorta: A Review of 505 Cases”, *Medicine*, Vol.37, (1958), pp.217-279.
- [31]Roberts, W.C., “Aortic Dissection: Anatomy Consequences and Causes”, *Am. Heart J.*, Vol.101, (1981), pp.195-214.
- [32]Macleod, R.I. and Soames, J.V., “Intimal Cushions in the Lingual Artery of Neonates and Children”, *Arch. Oral. Biol.*, Vol.30, (1985), pp.745-747.
- [33]Svensson, L.G. and Grawford, E.S., “Aortic dissection and Aortic Aneurysm Surgery: Clinical Observations, Experimental Investigations, and Statistical Analyses”, Part II. *Curr. Probl. Surg.*, Vol.29, (1992), pp.913-1057.
- [34]Wolinsky, H. and Glagov, S., “A lamellar unit of aortic medial structure and function in mammals”, *Circ. Res.*, Vol.20, (1967), pp.409-421.
- [35]van Baardwijk, C. Roach, M.R., “Factors in the propagation of aortic dissections in canine thoracic aortas”, *J. Biomech.*, Vol.20, (1987), pp.67-73.